journal of the mechanical behavior of biomedical materials 154 (2024) 106511

Contents lists available at ScienceDirect

Journal of the Mechanical Behavior of Biomedical Materials

journal homepage: www.elsevier.com/locate/jmbbm

Research paper

Nacre-like block lattice metamaterials with targeted phononic band gap and mechanical properties

Ravi Kiran Bollineni, Moustafa Sayed Ahmed, Shima Shahab *, Reza Mirzaeifar[1]

Department of Mechanical Engineering, Virginia Tech, Blacksburg, VA, 24061, USA

ARTICLE INFO

Keywords:
Bio-inspired materials
Block lattice metamaterials
Wave prorogation
Nacre-like metamaterials

ABSTRACT

The extraordinary quasi-static mechanical properties of nacre-like composite metamaterials, such as high specific strength, stiffness, and toughness, are due to the periodic arrangement of two distinct phases in a "brick and mortar" structure. It is also theorized that the hierarchical periodic structure of nacre structures can provide wider band gaps at different frequency scales. However, the function of hierarchy in the dynamic behavior of metamaterials is largely unknown, and most current investigations are focused on a single objective and specialized applications. Nature, on the other hand, appears to develop systems that represent a trade-off between multiple objectives, such as stiffness, fatigue resistance, and wave attenuation. Given the wide range of design options available to these systems, a multidisciplinary strategy combining diverse objectives may be a useful opportunity provided by bioinspired artificial systems. This paper describes a class of hierarchically-architected block lattice metamaterials with simultaneous wave filtering and enhanced mechanical properties, using deep learning based on artificial neural networks (ANN), to overcome the shortcomings of traditional design methods for forward prediction, parameter design, and topology design of block lattice metamaterial. Our approach uses ANN to efficiently describe the complicated interactions between nacre geometry and its attributes, and then use the Bayesian optimization technique to determine the optimal geometry constants that match the given fitness requirements. We numerically demonstrate that complete band gaps, that is attributed to the coupling effects of local resonances and Bragg scattering, exist. The coupling effects are naturally influenced by the topological arrangements of the continuous structures and the mechanical characteristics of the component phases. We also demonstrate how we can tune the frequency of the complete band gap by modifying the geometrical configurations and volume fraction distribution of the metamaterials. This research contributes to the development of mechanically robust block lattice metamaterials and lenses capable of controlling acoustic and elastic waves in hostile settings.

1. Introduction

Nacre, a natural composite material found in seashells that is composed of 95 volume percent inorganic plates (CaCO3) and 5 volume percent organic matrix (protein) in layered patterns, has long fascinated researchers for its unique highly organized structure and hierarchical construction. These provide nacre-like structures with superior material and physical qualities such as significantly better toughness (three orders of magnitude higher than monolithic aragonite) and energy absorption (Jackson et al., 1988; Espinosa et al., 2009; Chen et al., 2008). The brick-and-mortar structure of nacre's inner layers has evolved over millions of years to achieve these exceptional properties (Luz and Mano, 2009; Tang et al., 2003; Barthelat and Espinosa, 2007). In recent decades, researchers have successfully synthesized (Zhao and Guo, 2017; Gehrke et al., 2005; Corni et al., 2012; Yang et al., 2019; Yadav et al., 2018) nacre-inspired macroscopic structures for use in various applications such as engineering materials, super-capacitors, and nano-generators (Okumura and De Gennes, 2001; Neves and Mano, 2005; Studart, 2014). To construct artificial macroscopic materials, one viable strategy is to mimic the nacre's microscopic structure. This method could result in high-performance structural materials with numerous uses.

Brittle mineral bricks are combined with soft biological layers along two dimensions to form nacre brick-and-mortar constructions (Lu et al., 2022). Nacre's extraordinary toughness and other mechanical qualities are a result of the existence of the soft organic thin layers (Gao et al., 2017; Grossman et al., 2019; Mirzaeifar et al., 2015). Furthermore, the structure's periodic design and spatially variable elastic constants, which are comparable to acoustic metamaterials (Lu et al., 2009), allow

* Corresponding author.
E-mail address: sshahab@vt.edu (S. Shahab).
[1] This paper is dedicated to the memory of Prof. Reza Mirzaeifar passed away October 19, 2022.

https://doi.org/10.1016/j.jmbbm.2024.106511
Received 15 January 2024; Received in revised form 6 March 2024; Accepted 16 March 2024
Available online 18 March 2024

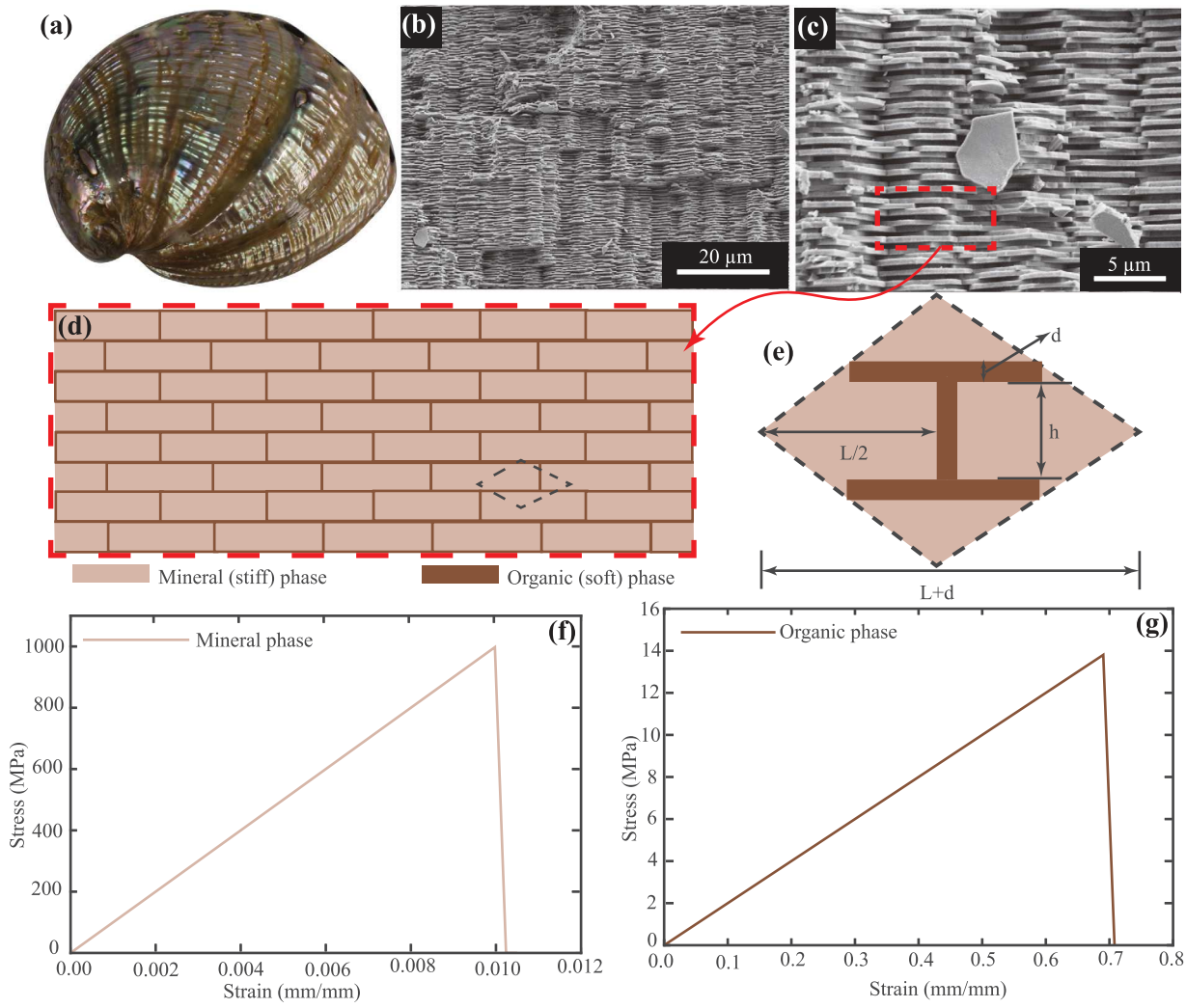

Fig. 1. (a) Picture of a abalone seashell showing shiny nacreous layer, (b, c) secondary SEM images of abalone shell (Haliotis rufescens), (d) nacre representative structure, (e) unit cell of nacre with various geometry parameters, (f) material behavior assigned to mineral phase, and (g) material behavior assigned to the organic phase.

it to manipulate mechanical wave propagation (Chen and Wang, 2015b, 2014). The phenomena of complete band gap (CBG) development within a specific frequency range, which originates from the nacre's microstructure organization, is of great interest. The large impedance mismatch between the mineral and organic phases caused by the nacre structure results in a wide band gap. The CBG specifies a frequency range in which waves are completely reflected, regardless of incident wave orientation (Chen and Wang, 2015a; Vadalà et al., 2018).

Several studies have been undertaken over the last decade to evaluate the mechanical properties of nacre structures utilizing experimental (Katti and Katti, 2006), numerical (Greco et al., 2020), and analytical methods (Cui et al., 2020). Computational and analytical approaches to studying CBG development in nacre-like structures have also been explored (Chen and Wang, 2014; Pranno et al., 2022). Additionally, numerous studies on the structure's microstructure optimization for the greatest toughness, stiffness, and a number of other mechanical properties are carried out. The microstructure of nacre has recently been the subject of much research in an effort to achieve the greatest potential material characteristics. These studies concentrated on the optimization of a specific target, usually the mechanical or wave attenuation. The fact that strong wave attenuation over broad band gaps is frequently coupled by poor mechanical properties is a significant disadvantage of band gap optimization in acoustic metamaterials (Chen and Wang, 2015a). Therefore, for applications operating in mechanically demanding situations, it is essential to design a framework that takes into account the mechanical and bad gap qualities. In this study, a novel multi-objective optimization technique is proposed to analyze trade-offs and obtain fair mechanical and band gap parameters.

Designing architected materials with the desired qualities is an inverse problem that is computationally expensive, and it is considerably more complicated when employing an experimental approach because this process requires trial and error, which is a more economically expensive process. However, several computational techniques have been developed in recent years as useful alternatives for precisely evaluating material properties at various length scales (Fish et al., 2021). Optimization methods have grown in popularity for designing materials with specific properties, but many of them, such as gradient-based optimization, require hundreds of simulations to evaluate the objective function, making them computationally expensive and prone to local optima (Ashby, 2000). Other optimization methods, such as Genetic Algorithm (GA) and mixed-variable programming, may necessitate hundreds of simulations before reaching a global optimum. Response surface approaches, while providing a thorough perspective of the variable design space, are frequently biased (Chakraborti et al., 2009). In contrast, Bayesian optimization (BO) offers an adaptive paradigm for more effectively sampling the design space and determining the overall best material design (Zhang et al., 2020). BO still calls for extensive simulations to evaluate the objective function, which can be computationally expensive when investigating changes to the

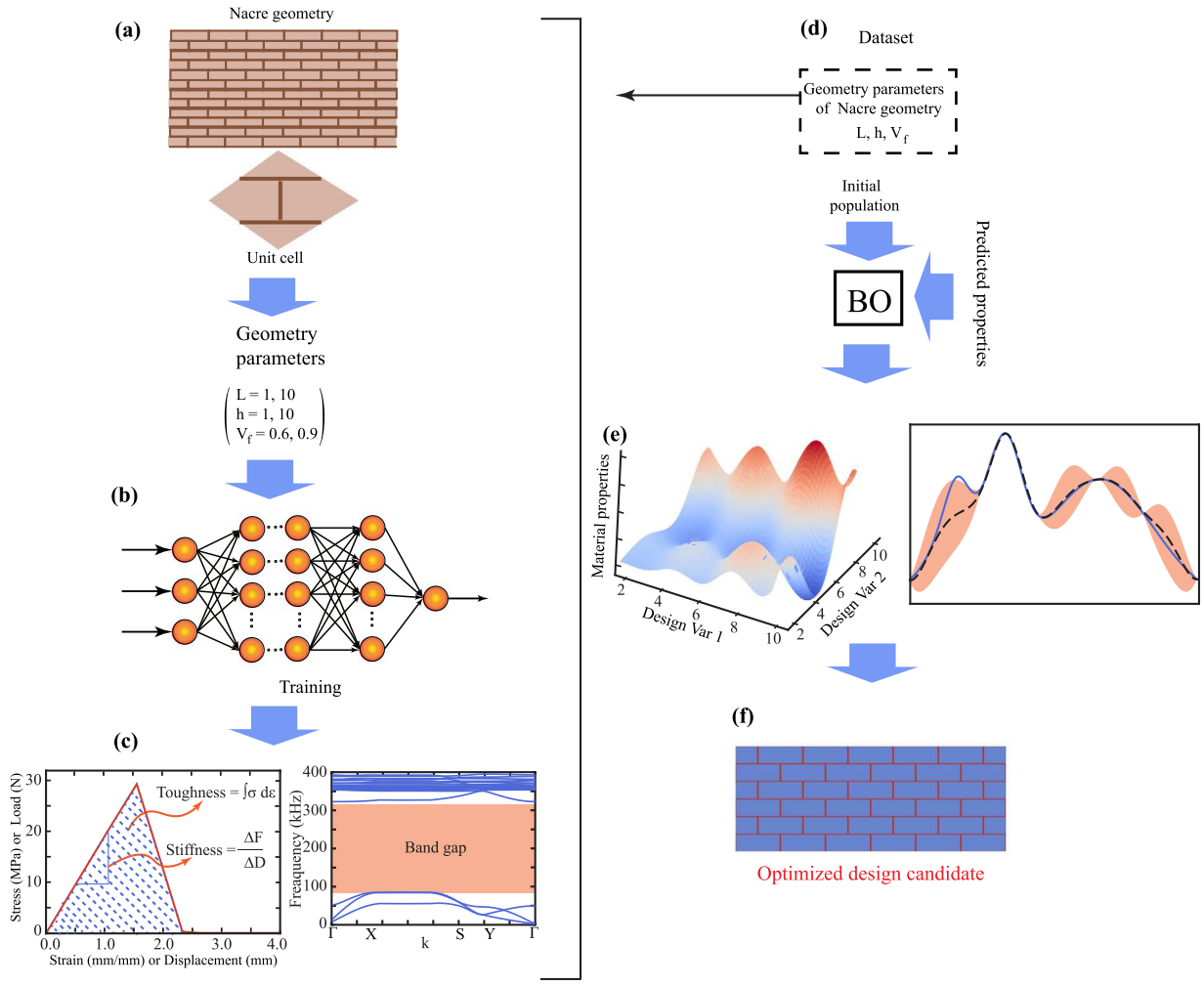

Fig. 2. (a) Nacre 2D geometry and unit cell, geometry parameters used in simulations, (b) ANN with input neurons, output neurons, and hidden layers, (c) mechanical properties and bandgap properties from the phonic crystal, (d) geometry dataset used as input to Bayesian optimization, (e) optimization surface after Bayesian optimization, and (f) optimized nacre geometry for the fitness function.

objective function. As a result, there is a need for effective and precise optimization methods that can reduce the amount of computation required to evaluate material parameters and objective functions. In this study, the proposed algorithm uses machine learning and BO techniques to significantly reduce the computational cost of microstructure optimization, making it a valuable tool for researchers interested in developing high-performance structural metamaterials for use in a variety of applications.

2. Unit cell analysis and methodology to inverse and forward design of the nacre lattice materials

Nacre is a one-of-a-kind periodic composite made up of multiple mineral plates embedded in an organic matrix. The image and secondary scanning electron microscopy (SEM) pictures at different sizes of the abalone shell (Haliotis rufescens) that illustrate the nacre like structure are shown in Fig. 1(a, b, and c). The representative front views of the nacre, as shown in Fig. 1(d), have a brick and mortar-like architecture, with a rhombus lattice that characterizes its two-dimensional microstructure. The length (L) of the mineral brick structure, the height (h) of the mineral layer, and the thickness (d) of the organic matrix in the x- and y-axis directions establish the lattice parameters of the nacre structure. Furthermore, the mineral phase volume fraction (V_f) in the unit is expressed as $V_f = Lh/((L + d)(h + d))$.

The nacre's unique three-dimensional staggered microstructure makes numerical modeling of the material behavior computationally demanding. To address this issue, a two-dimensional representative volume element (RVE) model is shown in Fig. 1(d, e) whose behavior is believed to represent the complete material. RVE models are used to assess the toughness, bending stiffness, and CBG of nacre. The material parameters given to the mineral phase and organic matrix of the nacre are shown in Fig. 1(f, g). The mineral phase's elastic modulus is 100 GPa, whereas the organic phase's is 20 MPa; both exhibit linear elastic brittle fracture material behavior. Furthermore, the stress–strain behavior of different phases reveals that the mineral phase is stiffer and has less ductility than the organic matrix. The following sections contain more information on the computational models.

For the inverse and forward design of the nacre lattice materials, a deep learning-based approach is proposed using desired material attributes as toughness, bending stiffness, and band gap. The potential influence of bio-inspired structures with superior mechanical and energy-absorbing qualities on real-world engineering applications serves as the driving force behind this study. The approach's major objective is to identify 2D unit cell designs with the most advantageous mechanical behavior and energy absorption characteristics. However, this proposed method's applications might be expanded to 3D structures or other fields (Zhang et al., 2022). For the sake of simplicity, all analyses are performed using 2D models, and geometries with all feasible combinations of lattice parameters are investigated in this work. The band gap is numerically calculated using the 2D unit cell presented in Fig. 1(e). A finite element (FE) study is carried out for

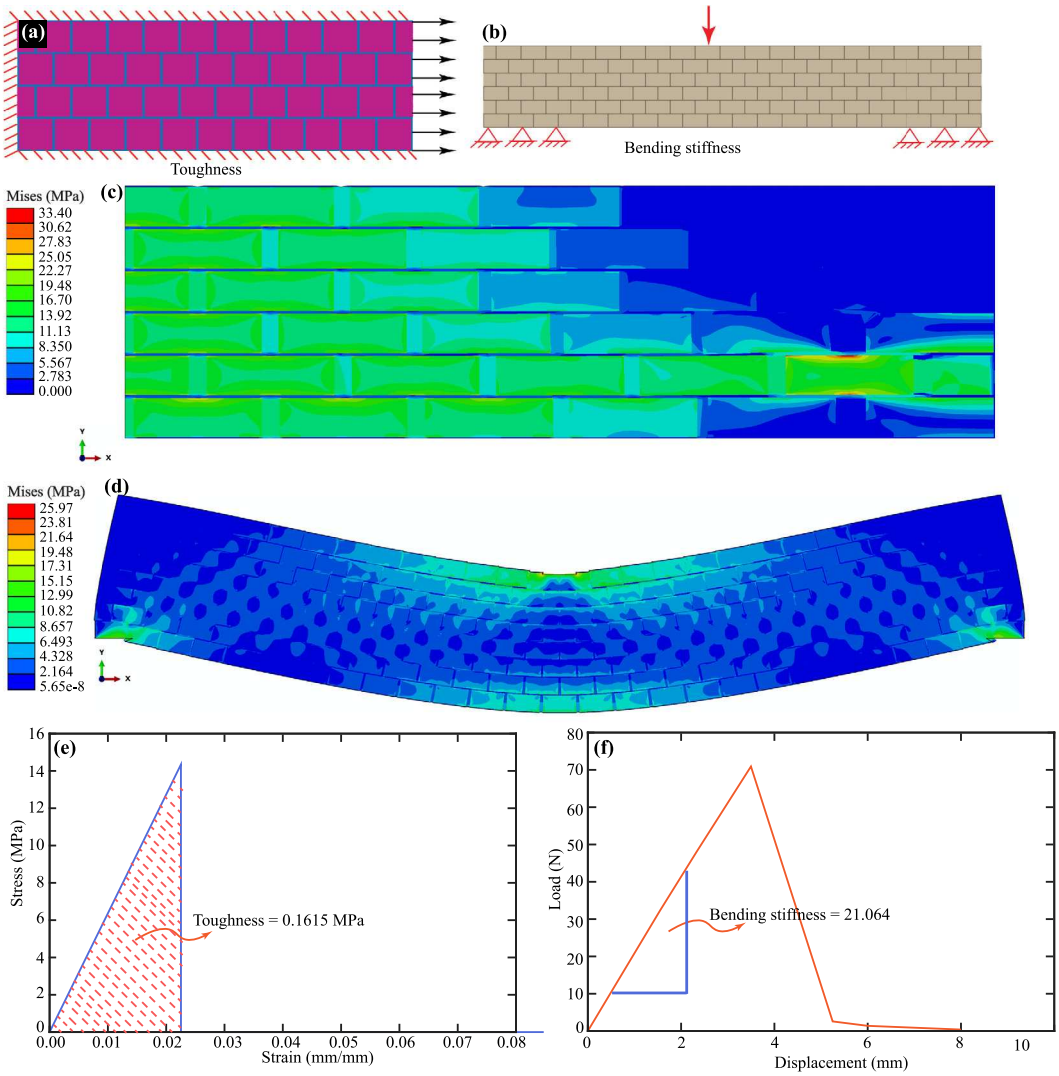

Fig. 3. (a, b) Finite element model setup used for simulating the toughness and bending, (c, d) Von Mises stress distribution for toughness and bending deformation in the models, (c) stress–strain curve from the toughness calculation simulations, and (d) load–displacement curve from the bending stiffness simulation calculation.

each nacre geometry, taking into account three cases: uniaxial test strength, three-point bending, and elastic wave propagation simulation. To compare alternative nacre geometries fairly, we assume constant density and material attributes for the mineral and organic phases. For a given set of material qualities, changes in nacre structure geometry parameters result in varying mechanical and band gap properties. The performance of the various structures is thus assessed using a fitness function that takes into account the effective properties due to varying loading and boundary conditions. The top-performing nacre structure is then chosen based on its fitness values and merged to form a unit cell, which may subsequently be tessellated to generate a periodic pattern.

Initially, the nacre structures are created in the computational framework with varied geometry parameters for the length and height of the brick, as well as the volume fraction of the mineral phase, as illustrated in Fig. 2(a). Then, on the resulting geometries, the corresponding FE simulations are run, and from those simulations, their material constants are determined as illustrated in Fig. 2(c). In order to train three neural networks for each network and material attribute, the geometrical parameters of the nacre and the evaluated materials constants are used as input and output parameters, respectively, as illustrated in Fig. 2(b). The details of network architectures and training are provided in the following sections. Indeed, the design space in our study consists of three parameters, yet our objective function involves multiple variables. To address this, we employed the BO technique to determine the optimal geometry for all three material parameters together. Finally, as illustrated in Fig. 2(d), the nacre shape is generated using the BO process with the specified material attributes. Instead of conducting the simulations, the output from the trained network is employed to lower the computational cost during the optimization phase. The geometry parameters are fed into the optimizer and then provided to the trained ANN networks during the nacre structure optimization phase. As demonstrated in Fig. 2(e), the predicted material properties are then used to fit the objective function. Finally, the optimizer returns the geometry parameters for fitting the objective functions, as shown in Fig. 2(f).

3. Stiffness and toughness mechanism of the nacre composite

The linear elastic brittle fracture material models are allocated to the mineral and organic phases of the structure in the FE simulations, with material constants specified in the manuscript. The unit cells are combined to have a rectangular geometry of a length of 50 mm and a height of 30 mm for evaluating the toughness. In the simulation, a static general step is assigned for toughness calculation. The model's loading and boundary conditions are as follows: the assembled model's left

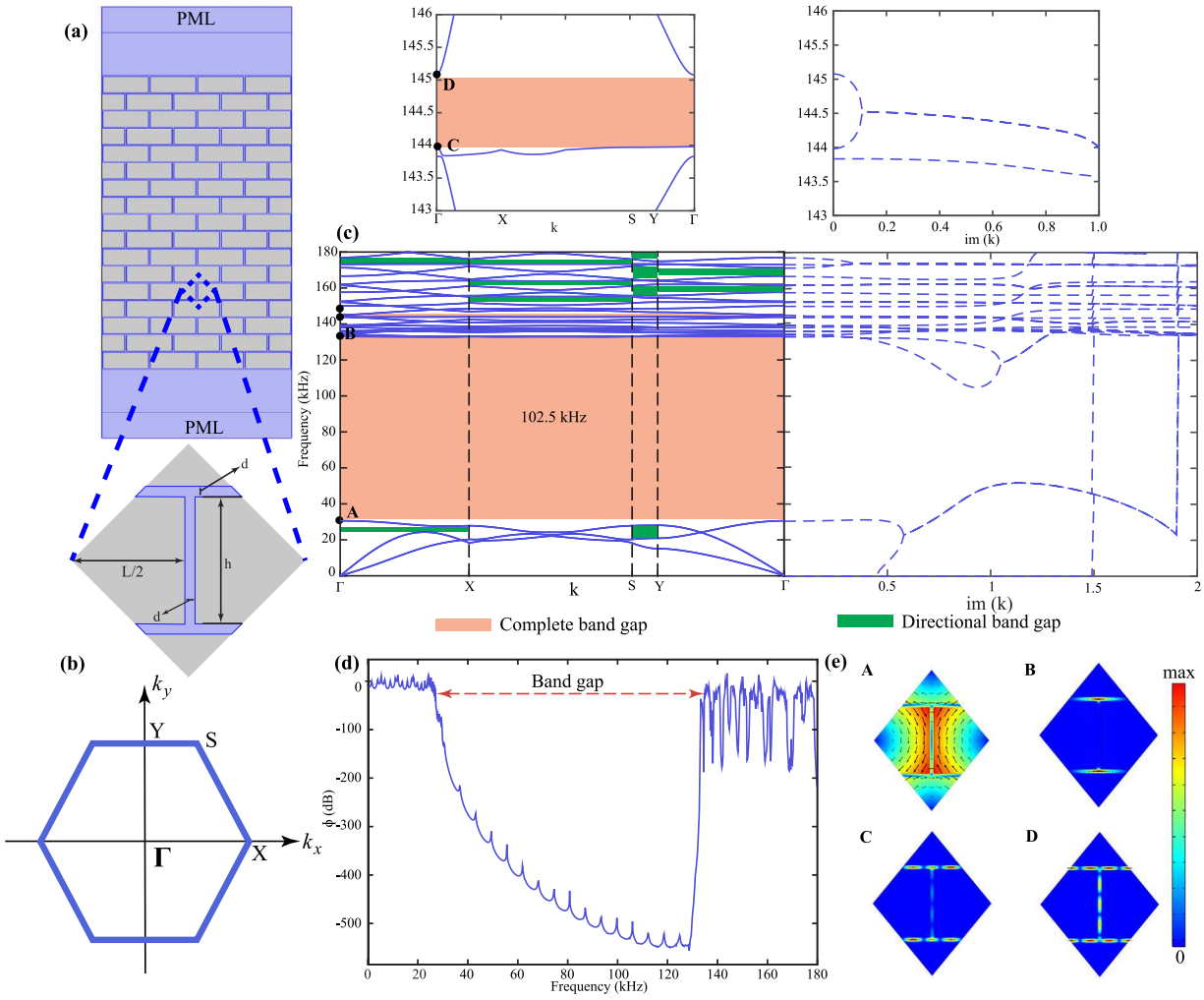

Fig. 4. (a) The nacre structure along with the unit cell used in this study, (b) The first Brillouin zone for the unit cell in (a) which is true for ($d \geq L - 2h$). The high symmetry points are defined as $\Gamma = (0, 0)$, $X = (\frac{\pi}{L+d} + \frac{\pi(L+d)}{4(h+d)^2}, 0)$, $S = (\frac{\pi}{L+d} - \frac{\pi(L+d)}{4(h+d)^2}, \frac{\pi}{h+d})$, $Y = (0, \frac{\pi}{h+d})$, (c) Unit cell optimization results of the band diagram showing an optimized complete band gap. The real and pure imaginary k vectors represent the propagating and evanescent waves passing through the unit cell. The subplots represent a zoomed region around the second complete band gap. (d) The transmission coefficient (ϕ) of the nacre structure showing a high attenuating band gap along the frequency of interest, (e) The contour plots of the total displacement fields of the eigenmodes highlighted in the band diagram in (c).

vertical edge is fixed in the x-direction, symmetric boundary conditions are applied to the top and bottom horizontal edges, and a positive displacement load along the x-axes is applied to the assembled model's right vertical edge as shown in Fig. 3(a). The distribution of Mises stresses in the mineral and organic phases of the nacre structure is depicted in Fig. 3(c). When both phases are deformed with a constant displacement simultaneously, less stress is concentrated in the softer phase than in the stiffer mineral phase, which is rational because the softer phase experiences less stress than the stiffer phase. The stress–strain curve is plotted as illustrated in Fig. 3(e) as a result of this simulation. The area under this curve is used to compute toughness for a specific nacre unit cell geometry.

A three-point bending simulation is used to test the bending stiffness of the nacre lattice. The global dimensions of the bulk beam model are 40 mm width and 200 mm length. These dimensions allowed us to incorporate a minimum of four layers of bricks in the vertical direction for a unit cell with a maximum width of 10 mm. However, considering a wider beam width was not an option since the unit cell width to 1 mm (minimum) in the vertical direction would necessitate 40 layers. Solving such a configuration would be computationally demanding. As a result, we used a fixed width of 40 mm for all cases to ensure consistency across all unit cell simulations and to minimize the edge effects indicated by Askarinejad et al. (2018), Alavi et al. (2022). The bottom borders of the beam's two sides are fixed in the x- and y-axes for three-point bending simulation, while a focused displacement of 10 mm along the y-axis is applied at the center of the beam as shown in Fig. 3(c). The Mises stress distribution, as illustrated in Fig. 3(d), is comparable to that of a traditional three-point bending beam, with stress concentration near the load action position and at the fixed edges. Stress is more concentrated in the mineral phase than in the soft organic layers, as demonstrated in the toughness simulation. The load–displacement plot illustrated in Fig. 3(f) is created by collecting reaction force and displacement from the load action edge. The slope of this curve is used to calculate the simulation's bending stiffness.

Using FE simulation approaches, we calculated the toughness and bending stiffness of the given unit cell dimensions. Subsequently, by assembling these unit cells, we determined the homogenized material properties of the entire nacre composite. However, it is important to note that these evaluated properties are specific to the alignment of the nacre unit cell with respect to the loading direction, for both toughness and bending stiffness cases (Peng et al., 2022). In this work, we did not consider these anisotropic behaviors however, we did consider the loading direction for both bending and tensile tests based on similar

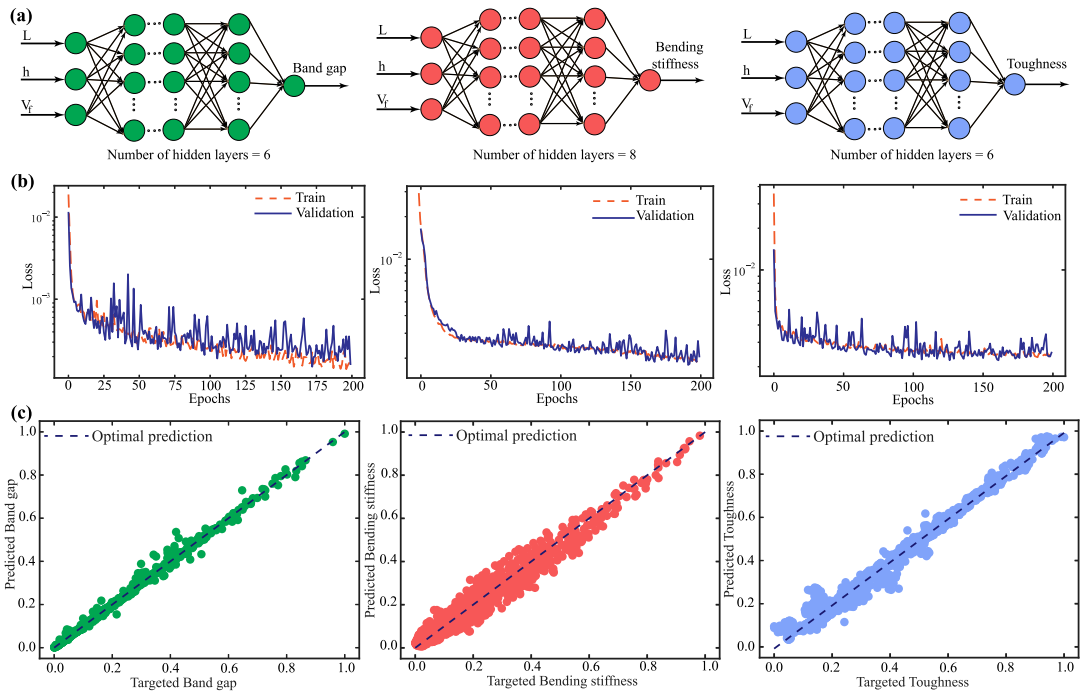

Fig. 5. (a) ANN networks used for training all three parameters, (b) training and validation losses for the three networks, and (c) predictions from the trained network.

works conducted on nacre composites to evaluate the overall material properties (Raj et al., 2020; Tang et al., 2022; Greco et al., 2020).

4. Physical mechanisms of the attenuation zones: local resonance and Bragg scattering

We employed composite Bloch's theorem to evaluate the band gap of the periodic nacre unit cell illustrated in Fig. 4(a), and Floquet periodic boundary conditions are applied to the unit cell boundaries. In this study, the FE approach is utilized to solve for the dispersion relations illustrated in the band diagram in Fig. 4(c) by scanning the reduced wave vector (k) in the first Brillouin zone along the symmetry path Γ-X-S-Y-Γ. Here "im" denotes a purely imaginary wavenumber. The band diagram is divided into branches that correspond to propagating (real k vector) and evanescent (pure imaginary k vector) waves. When the optimum parameters are used, a complete band gap opens up at the frequency range of 30–133 kHz, as shown in Fig. 4(c).

It is vital to understand that band gaps are formed by two mechanisms: Bragg scattering and local resonance. The constructive interference of reflected waves from various scatterings within the structure causes Bragg-band gaps. As a result, it is mostly determined by the periodicity of the nacre structure (Chen and Wang, 2014; Xiao et al., 2012; Raghavan and Phani, 2013). Local resonance band gaps, on the other hand, are caused by localized modes in the structure and hence only depend on the unit cell's resonance frequency (Chen and Wang, 2014; Raghavan and Phani, 2013; Sayed Ahmed et al., 2022; Ahmed et al., 2022). Red and green shaded spots show complete and directional band gaps, respectively. Directional band gaps happen when eigenvalues are undefined in specific directions, whereas full band gaps exist when no eigenvalues are defined in all directions of the irreducible Brillouin zone. The nacre structure's presumed non-symmetric unit cell causes directional band gaps induced by Bragg scattering (Cheng and Shi, 2014).

The optimized full band gap is thought to be the outcome of the coupling between Bragg scattering and local resonance in this study. The nature of the bands at real and imaginary wavenumbers, as seen in Fig. 4(c), supports this. For example, the bands at imaginary wavenumbers around the second complete band gap illustrated in the zoomed subplot at 144–145 kHz mimic a pattern often associated with Bragg band gaps (Krushynska et al., 2017).

Local resonance band gaps have a unique pattern of non-uniformly changing bands. Flat bands at real wavenumbers, on the other hand, show very confined modes (zero group velocity), implying the presence of local resonance. However, the structure of bands around a local resonant band gap is usually observed to exhibit a link between the flat dispersion of the resonator and the dispersion of the underlying medium (Liu and Hussein, 2012). As a result, Liu and Hussein (2012) establishes a unique criterion for local resonance by verifying the gradient of the group velocity $(\partial c_g/\partial k)$ where k is the dimensional wave number. A band gap bounded from above by an optical band is a local resonance band gap if $\partial c_g(\pi/d)/\partial k < 0$, where π/d indicates the Brillouin zone's X-point.

Fig. 4(e) shows the contour plots of the total normalized displacement fields of the eigenmodes highlighted in the band diagram in Fig. 4(c). The eigenmodes correspond to the boundaries of the complete band gaps. From Fig. 4(e)A, near Γ point, there exists a torsional mode in the mineral layer with average displacement in the organic layer. The wide band gap is bounded by mode B which represents a localized mode in the organic layer indicating a standing wave that prohibits energy transmission through the structure. This indicates the contribution of the local resonance to the optimized band gap. Likewise, modes C and D bands form the second band gap. Mode C shows a nearly flat band (standing wave) while mode D band is growing with the wavenumebr. Given the aforementioned conditions, this indicates that the wide band gap shown in Fig. 4(c) is a result of the coupling between Bragg scattering and local resonance band gaps. Bragg scattering mechanism dominates the formation of the second band gap according to the imaginary spectrum of the bands. For the incident displacement wave, the transmission coefficient is determined for a finite number of unit cells. As demonstrated in Fig. 4(a), an assembly of 4 × 8-unit cells sandwiched between the homogeneous organic matrix and perfectly matched layers (PML). The PMLs are employed at both ends of the uniform section to eliminate reflections caused by waves scattering at the boundaries of the domain. To calculate the transmission coefficient, a harmonic displacement of 10 nm amplitude is applied to the assembly

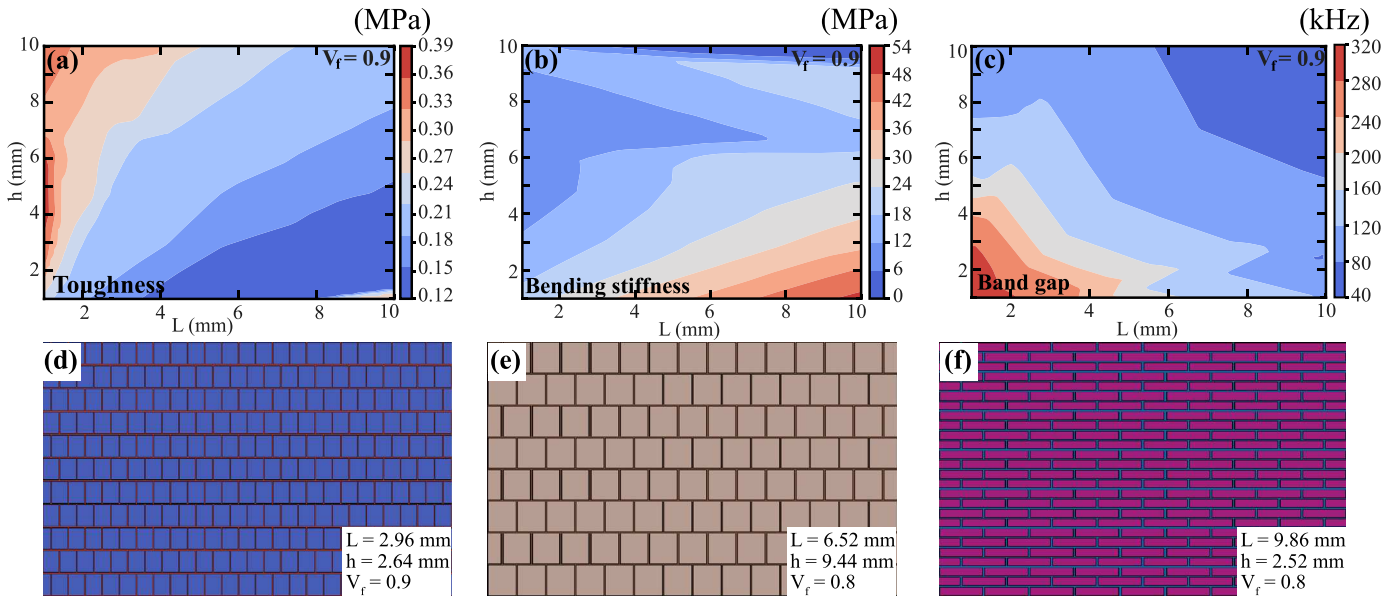

Fig. 6. (a, b, and c) Contour plots of toughness, bending stiffness, and bandgap with predicted values for V_f = 0.9 case, and (d, e, and f) sample geometries with varied unit cell parameters.

in the vertical direction. The transmission coefficient is calculated as follows:

$$\phi = 20\log\left[\left(|u| + |v|\right) / \left(|u_0| + |v_0|\right)\right] \tag{1}$$

Here u_0 and v_0 are incident displacements applied at the top interface between the organic layer and the PML layer, and u and v are horizontal and vertical displacements collected along the bottom interface between the organic homogeneous and PML layer. The frequency domain is swept from 0 to 180 KHz, as shown in 4(d). The band gap shown in Fig. 4(c) indicates that both values are in good agreement. This demonstrates the potential applicability of the finite periodic composite by confirming the reliability of the simulated complete band gaps in the band structure using the Bloch theorem. Fig. 4(f) depicts the absolute displacement in the finite nacre assembly at the same frequencies as the unit cell.

5. Artificial neural networks training and predictions

Approximately 2000 simulations are conducted to analyze various simulation data for training the ANN's, covering a range of brick length and height from 1 to 10 mm and mineral phase volume fractions from 0.6 to 0.9. Two Python scripts are employed to take the geometry parameters as inputs and simulate all of these models in ABAQUS, estimating the values of toughness and bending stiffness. Additionally, a MATLAB script performs simulations in COMSOL using the given geometry parameters as inputs and calculates the associated band gap property. The automation strategy streamlines the simulation and data collection processes.

In this work, three fully connected ANN networks are utilized to predict the material properties of the nacre structure. The dimensional vector consists of geometry parameters (L, h, and V_f) are passed through the input layer. The input vector (geometry parameters, x_j) is passed through the input layer and the passing through the hidden layers to generate the output vector (material properties y_j) using the following relation (Riedmiller, 1994).

$$y_j = f\left(\sum_j W_{ij}x_j + b_i\right) \tag{2}$$

Here, W_{ij} and b_i are the weights and biases between the layers, and f is the non-linear activation function. The ANN networks as shown in Fig. 5(a) with the specified number of hidden layers with varying number of neurons in each layer and use the ReLU activation function. The mean squared error (MSE) is employed to evaluate the difference between the predictive value and the ground truth material property. The gradient based weight update step at the end of each training step is given as.

$$\alpha_{n+1} = \alpha_n - \eta.\nabla_\alpha MSE\left(\alpha_n\right) \tag{3}$$

Here n refers to the number of iterations used for fitting the function, and α refers to the weights and biases, and η is the learning rate. Using the above relationship, the weights and biases are changed iteratively. The Adam (Kingma and Adam, 2014) optimizer is used to train the ANN networks with a learning rate of 10^{-3}. The ANN networks are trained over 200 epochs with varying batch sizes. When the model trains through the whole training dataset of 1800 data points, the remaining 200 data points are used to evaluate the validation losses for training the network. The training and validation loss of the three ANN networks are depicted in Fig. 5(b). The predictions that match the expected outputs of the trained networks are shown in Fig. 5(c). Keras is used to train and build all of the networks (Gulli and Pal, 2017).

6. Effects of mineral layer dimensions on phononic band gaps and mechanical properties

The trained ANN networks were used to create the contour plots for each material attribute, such as toughness, bending stiffness, and band gap, as shown in Fig. 6(a, b, and c). To achieve this, the length (L) and height (h) for a certain volume fraction instance with Vf = 0.9 were changed. The toughness of the nacre structure is high for small length and higher breadth mineral bricks in the contour plots for V_f = 0.9 scenario. This is mostly because the organic layer thickness values for this design are smaller. Bending stiffness, on the other hand, follows a nearly opposite pattern to toughness, with higher stiffness reported for mineral bricks of greater length and smaller breadth. The complete band gap, on the other hand, follows a completely different trend, with larger frequency band gaps for smaller length and breadth bricks. This phenomenon can be explained by the observation that as the thickness

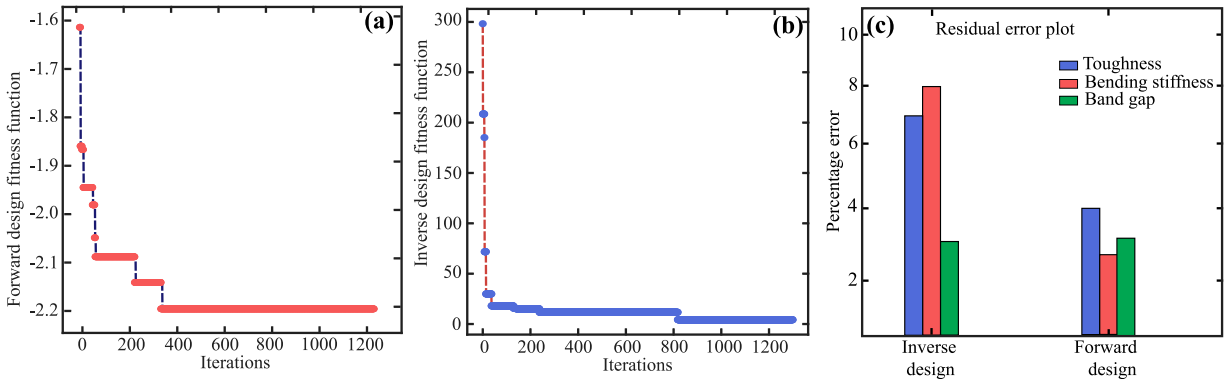

Fig. 7. (a),(b) Bayesian optimization curves for forward and inverse design, and (c) residual error between the predicted and simulated properties.

of the organic layer is lowered, the band gap increases. Furthermore, upon comparing the contour plots of the three material properties, a notable symmetry is observed in the band gap property along the line traversing between (L = 0, h = 0) and (L = 10, h = 10). This symmetry arises from the consideration of wave directional anisotropy in the band gap simulation calculation. However, such symmetry is not observed in the toughness and bending stiffness contour plots, attributable to the omission of these anisotropic behaviors concerning the loading direction, as explained in the simulation section. The contour plots clearly show that optimizing the nacre geometry for desired material attributes is a difficult optimization task, especially when one of the nacre geometry parameter volume fractions varies discretely. As a result, employing gradient-based optimization to estimate the geometrical parameters of the nacre while also determining ideal material constants may be impractical. The produced geometries with varied unit cell parameters are shown in Fig. 6(d, e, and f).

7. Bayesian optimization for inverse and forward design of the nacre composite

We present a Gaussian-based Bayesian-based optimization approach for solving forward and inverse design optimization issues in this paper. In this optimization step, function evaluations were performed using the trained ANN network, eliminating the need to run computationally expensive physical finite element simulations. This strategy greatly decreases optimization time, taking only a few minutes to solve a problem that would otherwise take several hours to solve using the direct approach. The Gaussian technique is used first to pick the input geometry parameters, which are determined by the fitness function and domain space. Two problems are considered to demonstrate the potential of the proposed computational technique. The first one is the inverse problem, which entails directly optimizing the geometry parameters for the desired material constants. The second problem in forward design is to optimize the geometry for the optimal material parameters.

The fitness function utilized in this study for Bayesian optimization for forward and inverse design is defined by the following Eqs. (4) and (5), respectively.

$$FD = \max\left(\log\left(\frac{T_{pred}-T_{min}}{T_{max}-T_{min}}\right)+\log\left(\frac{BS_{pred}-BS_{min}}{BS_{max}-BS_{min}}\right)+\log\left(\frac{BG_{pred}-BG_{min}}{BG_{max}-BG_{min}}\right)\right) \tag{4}$$

$$ID = \min\left(\frac{|T_{pred}-T_{target}|}{T_{target}}+\frac{|BS_{pred}-BS_{target}|}{BS_{target}}+\frac{|BG_{pred}-BG_{target}|}{BG_{target}}\right) \tag{5}$$

The optimization is aimed to maximize and minimize the three independent parameters in the multi-objective functions found in Eqs. (4) and (5). Fig. 7(a, b) depicts the objective function fitting in each iteration for both inverse and forward design. From the optimization curves it reveals that the forward design objective function was evaluated 350 times, while the inverse design objective function required 800 evaluations by the trained ANN to reach the optimal values during the optimization process. The results are validated using direct simulation results, and the residual error determined for both scenarios between simulation and predicted results from trained ANN is given in Fig. 7(c) as a bar plot. The bar plot clearly shows that the error percentage for all parameters is less than 10 percent. The nacre structure with the appropriate material qualities can be generated with minimal computational time by employing these trained networks and the Bayesian optimization process. The proposed method holds a lot of promise for solving complex optimization problems in materials design.

8. Conclusions

In order to address the drawbacks of conventional design methods for forward prediction, parameter design, and topology design of metamaterials, this paper describes a class of hierarchically-architected block lattice metamaterials with simultaneous wave filtering and enhanced mechanical properties. In our method, artificial neural networks were used to effectively explain the complex connections between nacre geometry and its properties, and the best geometry constants that satisfy the specified fitness requirements were subsequently found using the BO strategy. The method was demonstrated to be a computationally efficient strategy for altering the nacre structure to achieve optimal material properties. The suggested approach not only allows for forward design of the nacre structure, but it also allows for structure design for selected material constants by significantly altering the fitness function of the optimization process. This method is not only applicable to the design of nacre structures; it can also be used to solve many design optimization problems for artificial metamaterials, enhancing material design for desired material constants that can be confirmed with experimental findings in separate communications. Overall, the proposed method appears to be a potential tool for developing materials with precise desired features while minimizing computing costs. The methodology can be a valuable resource for materials scientists, engineers, and designers who want to improve material performance and contribute to the creation of new architected acoustic materials and holographic lenses (Bakhtiari-Nejad et al., 2018).

CRediT authorship contribution statement

Ravi Kiran Bollineni: Writing – original draft, Visualization, Validation, Software, Methodology, Investigation, Formal analysis, Data curation, Conceptualization. **Moustafa Sayed Ahmed:** Writing – original

draft, Validation, Software, Investigation, Formal analysis. **Shima Shahab:** Writing – review & editing, Supervision, Resources, Project administration, Methodology, Investigation, Funding acquisition, Conceptualization. **Reza Mirzaeifar:** Writing – original draft, Visualization, Supervision, Resources, Methodology, Investigation, Funding acquisition, Conceptualization.

Declaration of competing interest

The authors declare the following financial interests/personal relationships which may be considered as potential competing interests: Shima Shahab reports financial support was provided by Virginia Polytechnic Institute and State University. Shima Shahab reports a relationship with Virginia Polytechnic Institute and State University that includes: employment. If there are other authors, they declare that they have no known competing financial interests or personal relationships that could have appeared to influence the work reported in this paper.

Data availability

Data will be made available on request.

Acknowledgments

MSA and SS were supported by the U.S. National Science Foundation (NSF) under the CAREER grant, Award No. CMMI 2143788, which is gratefully acknowledged. The authors would like to thank Dr. Ling Li, and Dr. Zhifei Deng for providing the pictures and secondary SEM images of a Abalone seashells.

References

Ahmed, M.A.S., Robert, B., Ghommem, M., Shahab, S., 2022. Genetic algorithm optimization for through-wall ultrasound power transfer systems. In: Active and Passive Smart Structures and Integrated Systems XVI. SPIE.

Alavi, S., Ganghoffer, J., Sadighi, M., Nasimsobhan, M., Akbarzadeh, A., 2022. Continualization method of lattice materials and analysis of size effects revisited based on cosserat models. Int. J. Solids Struct. 254, 111894.

Ashby, M., 2000. Multi-objective optimization in material design and selection. Acta Mater. 48 (1), 359–369.

Askarinejad, S., Choshali, H.A., Flavin, C., Rahbar, N., 2018. Effects of tablet waviness on the mechanical response of architected multilayered materials: Modeling and experiment. Compos. Struct. 195, 118–125.

Bakhtiari-Nejad, M., Elnahhas, A., Hajj, M.R., Shahab, S., 2018. Acoustic holograms in contactless ultrasonic power transfer systems: Modeling and experiment. J. Appl. Phys. 124 (24).

Barthelat, F., Espinosa, H., 2007. An experimental investigation of deformation and fracture of nacre–mother of pearl. Exp. Mech. 47, 311–324.

Chakraborti, N., Sreevathsan, R., Jayakanth, R., Bhattacharya, B., 2009. Tailor-made material design: An evolutionary approach using multi-objective genetic algorithms. Comput. Mater. Sci. 45 (1), 1–7.

Chen, Y., Wang, L., 2014. Tunable band gaps in bio-inspired periodic composites with nacre-like microstructure. J. Appl. Phys. 116 (6), 063506.

Chen, Y., Wang, L., 2015a. Bio-inspired heterogeneous composites for broadband vibration mitigation. Sci. Rep. 5 (1), 17865.

Chen, Y., Wang, L., 2015b. Multiband wave filtering and waveguiding in bio-inspired hierarchical composites. Extreme Mech. Lett. 5, 18–24.

Chen, R., Wang, C.-a., Huang, Y., Le, H., 2008. An efficient biomimetic process for fabrication of artificial nacre with ordered-nanostructure. Mater. Sci. Eng. C 28 (2), 218–222.

Cheng, Z., Shi, Z., 2014. Vibration attenuation properties of periodic rubber concrete panels. Constr. Build. Mater. 50, 257–265.

Corni, I., Harvey, T., Wharton, J., Stokes, K., Walsh, F., Wood, R., 2012. A review of experimental techniques to produce a nacre-like structure. Bioinspiration Biomimetics 7 (3), 031001.

Cui, S., Yang, Z., Lu, Z., 2020. An analytical model for the bio-inspired nacreous composites with interlocked "brick-and-mortar" structures. Compos. Sci. Technol. 193, 108131.

Espinosa, H.D., Rim, J.E., Barthelat, F., Buehler, M.J., 2009. Merger of structure and material in nacre and bone–Perspectives on de novo biomimetic materials. Prog. Mater. Sci. 54 (8), 1059–1100.

Fish, J., Wagner, G.J., Keten, S., 2021. Mesoscopic and multiscale modelling in materials. Nature Mater. 20 (6), 774–786.

Gao, H.-L., Chen, S.-M., Mao, L.-B., Song, Z.-Q., Yao, H.-B., Cölfen, H., Luo, X.-S., Zhang, F., Pan, Z., Meng, Y.-F., et al., 2017. Mass production of bulk artificial nacre with excellent mechanical properties. Nat. Commun. 8 (1), 287.

Gehrke, N., Nassif, N., Pinna, N., Antonietti, M., Gupta, H.S., Cölfen, H., 2005. Retrosynthesis of nacre via amorphous precursor particles. Chem. Mater. 17 (26), 6514–6516.

Greco, F., Leonetti, L., Pranno, A., Rudykh, S., 2020. Mechanical behavior of bio-inspired nacre-like composites: A hybrid multiscale modeling approach. Compos. Struct. 233, 111625.

Grossman, M., Pivovarov, D., Bouville, F., Dransfeld, C., Masania, K., Studart, A.R., 2019. Hierarchical toughening of nacre-like composites. Adv. Funct. Mater. 29 (9), 1806800.

Gulli, A., Pal, S., 2017. Deep Learning with Keras. Packt Publishing Ltd.

Jackson, A., Vincent, J.F., Turner, R., 1988. The mechanical design of nacre. Proc. R. Soc. Lond. [Biol.] 234 (1277), 415–440.

Katti, K.S., Katti, D.R., 2006. Why is nacre so tough and strong? Mater. Sci. Eng. C 26 (8), 1317–1324.

Kingma, D.P., Adam, B.J., 2014. A method for stochastic optimization. arxiv preprint 2014. 205 arXiv preprint arXiv:1412.6980.

Krushynska, A.O., Miniaci, M., Bosia, F., Pugno, N.M., 2017. Coupling local resonance with Bragg band gaps in single-phase mechanical metamaterials. Extreme Mech. Lett. 12, 30–36.

Liu, L., Hussein, M.I., 2012. Wave motion in periodic flexural beams and characterization of the transition between Bragg scattering and local resonance. J. Appl. Mech. 79 (1).

Lu, M.-H., Feng, L., Chen, Y.-F., 2009. Phononic crystals and acoustic metamaterials. Mater. Today 12 (12), 34–42.

Lu, Y., Huang, G.-Y., Wang, Y.-F., Wang, Y.-S., 2022. A mechanical model for elastic wave propagation in nacre-like materials with brick-and-mortar microstructures. J. Appl. Mech. 89 (9), 091002.

Luz, G.M., Mano, J.F., 2009. Biomimetic design of materials and biomaterials inspired by the structure of nacre. Phil. Trans. R. Soc. A 367 (1893), 1587–1605.

Mirzaeifar, R., Dimas, L.S., Qin, Z., Buehler, M.J., 2015. Defect-tolerant bioinspired hierarchical composites: simulation and experiment. ACS Biomater. Sci. Eng. 1 (5), 295–304.

Neves, N., Mano, J., 2005. Structure/mechanical behavior relationships in crossed-lamellar sea shells. Mater. Sci. Eng. C 25 (2), 113–118.

Okumura, K., De Gennes, P.-G., 2001. Why is nacre strong? Elastic theory and fracture mechanics for biocomposites with stratified structures. Eur. Phys. J. E 4, 121–127.

Peng, X.-L., Lee, S., Wilmers, J., Oh, S.H., Bargmann, S., 2022. Orientation-dependent micromechanical behavior of nacre: In situ TEM experiments and finite element simulations. Acta Biomater. 147, 120–128.

Pranno, A., Greco, F., Leonetti, L., Lonetti, P., Luciano, R., De Maio, U., 2022. Band gap tuning through microscopic instabilities of compressively loaded lightened nacre-like composite metamaterials. Compos. Struct. 282, 115032.

Raghavan, L., Phani, A.S., 2013. Local resonance bandgaps in periodic media: Theory and experiment. J. Acoust. Soc. Am. 134 (3), 1950–1959.

Raj, M., Patil, S.P., Markert, B., 2020. Mechanical properties of nacre-like composites: A bottom-up approach. J. Compos. Sci. 4 (2), 35.

Riedmiller, M., 1994. Advanced supervised learning in multi-layer perceptrons—from backpropagation to adaptive learning algorithms. Comput. Stand. Interfaces 16 (3), 265–278.

Sayed Ahmed, M., Ghommem, M., Shahab, S., 2022. Mode couplings in multiplex electromechanical structures. J. Appl. Phys. 132 (12).

Studart, A.R., 2014. Turning brittleness into toughness. Nature Mater. 13 (5), 433–435.

Tang, Z., Kotov, N.A., Magonov, S., Ozturk, B., 2003. Nanostructured artificial nacre. Nature Mater. 2 (6), 413–418.

Tang, B., Niu, S., Yang, J., Shao, C., Wang, M., Ni, J., Zhang, X., Yang, X., 2022. Investigation of bioinspired nacreous structure on strength and toughness. Biomimetics 7 (3), 120.

Vadalà, F., Bacigalupo, A., Lepidi, M., Gambarotta, L., 2018. Bloch wave filtering in tetrachiral materials via mechanical tuning. Compos. Struct. 201, 340–351.

Xiao, Y., Wen, J., Wen, X., 2012. Broadband locally resonant beams containing multiple periodic arrays of attached resonators. Phys. Lett. A 376 (16), 1384–1390.

Yadav, R., Goud, R., Dutta, A., Wang, X., Naebe, M., Kandasubramanian, B., 2018. Biomimicking of hierarchal molluscan shell structure via layer by layer 3D printing. Ind. Eng. Chem. Res. 57 (32), 10832–10840.

Yang, Y., Li, X., Chu, M., Sun, H., Jin, J., Yu, K., Wang, Q., Zhou, Q., Chen, Y., 2019. Electrically assisted 3D printing of nacre-inspired structures with self-sensing capability. Sci. Adv. 5 (4), eaau9490.

Zhang, Y., Apley, D.W., Chen, W., 2020. Bayesian optimization for materials design with mixed quantitative and qualitative variables. Sci. Rep. 10 (1), 1–13.

Zhang, X., Wu, K., Ni, Y., He, L., 2022. Anomalous inapplicability of nacre-like architectures as impact-resistant templates in a wide range of impact velocities. Nature Commun. 13 (1), 7719.

Zhao, H., Guo, L., 2017. Nacre-inspired structural composites: performance-enhancement strategy and perspective. Adv. Mater. 29 (45), 1702903.